

1 **First studies of mesosphere and lower thermosphere**
2 **dynamics using a multistatic specular meteor radar**
3 **network over southern Patagonia**

4 **J. Federico Conte¹, Jorge L. Chau¹, J. Miguel Urco^{1,2}, Ralph Latteck¹, Juha**
5 **Vierinen⁵, and Jacobo O. Salvador^{3,4}**

6 ¹Leibniz Institute of Atmospheric Physics at the University of Rostock, Kühlungsborn, Germany

7 ²Department of Electrical and Computer Engineering and Coordinated Science Laboratory, University of

8 Illinois at Urbana-Champaign, Urbana, IL, USA

9 ³Universidad Nacional de la Patagonia Austral, Río Gallegos, Argentina

10 ⁴CONICET, Argentina

11 ⁵Arctic University of Norway, Tromsø, Norway

12 **Key Points:**

- 13 • First observations of MLT dynamics over one of the most dynamically active re-
- 14 gions in the world
- 15 • Estimates of mean horizontal winds and their gradients are possible, thanks to the
- 16 multistatic configuration.
- 17 • Mean momentum fluxes are estimated with vertical velocity estimates free of hor-
- 18 izontal divergence contamination.

Corresponding author: J. Federico Conte, conte@iap-kborn.de

19 **Abstract**

20 This paper presents for the first time results on winds, tides, gradients of horizontal
 21 winds, and momentum fluxes at mesosphere and lower thermosphere (MLT) altitudes
 22 over southern Patagonia, one of the most dynamically active regions in the world. For
 23 this purpose, measurements provided by SIMONe Argentina are investigated. SIMONe
 24 Argentina is a novel multistatic specular meteor radar system that implements a SIMONe
 25 (Spread Spectrum Interferometric Multistatic meteor radar Observing Network) approach,
 26 and that has been operating since the end of September 2019. Average counts of more
 27 than 30000 meteor detections per day result in tidal estimates with statistical uncertain-
 28 ties of less than 1 m/s. Thanks to the multistatic configuration, horizontal and vertical
 29 gradients of the horizontal winds are obtained, as well as vertical winds free from hor-
 30 izontal divergence contamination. The vertical gradients of both zonal and meridional
 31 winds exhibit strong tidal signatures. Mean momentum fluxes are estimated after remov-
 32 ing the effects of mean winds using a four-hour, eight-kilometer window in time and al-
 33 titude, respectively. Reasonable statistical uncertainties of the momentum fluxes are ob-
 34 tained after applying a 28-day averaging. Therefore, the momentum flux estimates pre-
 35 sented in this paper represent monthly mean values of waves with periods of four hours
 36 or less, vertical wavelengths shorter than eight kilometers, and horizontal scales less than
 37 400 km.

38 **1 Introduction**

39 The mesosphere and lower thermosphere (MLT) is the atmospheric region that cou-
 40 ples the lower and upper parts of the terrestrial atmosphere. For this reason, knowledge
 41 of its dynamics is of great importance in order to understand the behavior of the atmo-
 42 sphere as a whole. The coupling is accomplished mainly via propagation of three dom-
 43 inant types of waves: planetary waves (PWs), tides, and gravity waves (GWs). PWs are
 44 waves with scales of thousands of kilometers and periods of up to ~ 30 days. They are
 45 mainly generated in the troposphere by land-sea discontinuities, or triggered in-situ by,
 46 e.g., baroclinic instabilities and filtered gravity waves (e.g., Rossby, 1939; McCormack
 47 et al., 2014; H.-L. Liu & Roble, 2002). Tides are also waves with horizontal scales of thou-
 48 sands of kilometers, but periods that are sub-harmonics of the solar and lunar days. Ther-
 49 mal tides are mainly a consequence of solar radiation absorption by water vapour in the
 50 troposphere and ozone in the stratosphere, while the lunar tide results from the grav-
 51 itational pull of the Moon (e.g., Lindzen & Chapman, 1969; Forbes, 1984). GWs are small
 52 to medium scale waves with periods ranging from about 5 minutes to many hours. They
 53 can be triggered by a myriad of different sources, e.g., the orography, thunderstorms, shear
 54 instabilities, convection, etc. (e.g., Hines, 1988; Piani et al., 2000; Fritts & Alexander,
 55 2003).

56 During the last decades, specular meteor radars (SMRs) have been extensively used
 57 to study winds and atmospheric waves in the MLT (e.g., Hocking, 2005; Clemesha et al.,
 58 2009; Hoffmann et al., 2010; A. Z. Liu et al., 2013; Laskar et al., 2016; Jia et al., 2018,
 59 and references therein). They have also been used to study GWs, which are known to
 60 play an important role in determining the wind and thermal structure of the MLT (e.g.,
 61 Fritts, 1984). Particularly, some studies have focused on extracting information about
 62 GW-driven momentum fluxes from SMR measurements (e.g., Fritts et al., 2010; Placke
 63 et al., 2011a; Andrioli et al., 2015). However, understanding the results on momentum
 64 flux estimates based on SMR winds is not trivial, mainly because of the uncertainties
 65 associated with the estimation procedure (e.g., Fritts et al., 2012b). In fact, Vincent et
 66 al. (2010) showed that the accuracy in the momentum flux estimation is highly depen-
 67 dent on the number of meteor detections. Consequently, the usage of multistatic meteor
 68 radar systems represents one way to reduce the uncertainties of the momentum flux es-
 69 timates (e.g., Spargo et al., 2019). Furthermore, by detecting more meteors and being

70 able to observe them from different viewing points, multistatic SMR systems also allow
71 for more reliable estimations of horizontal wind gradients.

72 The MLT over the southern part of Argentina and Chile is considered to be one
73 of the most dynamically active regions in the globe. Satellite-based studies have revealed
74 that GW-driven momentum fluxes increase considerably at both stratosphere and MLT
75 altitudes over Patagonia (e.g., Trinh et al., 2018; Vadas et al., 2019a). Numerical model
76 simulations have reported generation of secondary GWs with horizontal scales of up to
77 2000 km at mesospheric altitudes over the southern Andes (Vadas & Becker, 2019). Nev-
78 ertheless, wave coupling processes in the MLT region over the Patagonian sector are still
79 not well understood, partly because the installation of ground-based instruments has not
80 been possible, either due to logistics challenges or instrument requirements. In this work,
81 we present preliminary results of a multistatic SMR network that allows, for the first time,
82 measurements of MLT dynamics in the Patagonian region. Besides the local support,
83 our success has been possible thanks to a novel approach that we call SIMONe (Spread
84 Spectrum Interferometric Multistatic meteor radar Observing Network) (Chau et al., 2019).
85 SIMONe makes use of modern radar practices like spread-spectrum, MIMO (Multiple-
86 Input, Multiple-Output), and compressed sensing applied to atmospheric radars (Vierinen
87 et al., 2016; Urco et al., 2018, 2019). This allows for much easier installation, operation
88 and expansion of the network than previous equivalent systems.

89 The paper is organized as follows. Section 2 introduces the SIMONe Argentina sys-
90 tem. Section 3 provides a detailed description of the different analyses performed to the
91 data. The main results and findings are presented and discussed in Section 4. Finally,
92 the concluding remarks are provided in section 5.

93 2 SIMONe Argentina

94 SIMONe Argentina is a state-of-the-art network of multistatic specular meteor radars
95 that was installed in September of 2019 in the southern province of Santa Cruz, Argentina.
96 It is comprised of one single transmitting site with five linearly polarized Yagi antennas
97 in a pentagon configuration, and five receiving sites with one dual-polarization Yagi an-
98 tenna each. The receivers are placed between 30 and 270 km of distance from the trans-
99 mitting site, which is located at 49.6° S, 71.4° W (see Figure 1 for details on the geo-
100 graphical distribution of the sites). This type of network configuration is known as MISO
101 (Multiple-Input, Single-Output), since only one antenna is used on reception (e.g., Chau
102 et al., 2019).

103 SIMONe Argentina is the result of an effort led by the Leibniz Institute of Atmo-
104 spheric Physics (Germany) in collaboration with the Universidad Nacional de la Patag-
105 onia Austral (Argentina), and the Arctic University of Norway. A similar system has been
106 installed in Peru (SIMONe Peru). SIMONe systems use coded spread spectrum on trans-
107 mission (Vierinen et al., 2016). A phase coded signal based on pseudo-random sequences
108 is generated and transmitted on each antenna independently. Transmission is done at
109 a frequency of 32.55 MHz and with an average power of 400 W per antenna. All five trans-
110 mitted codes are simultaneously decoded at each receiving site by means of compressed
111 sensing (e.g., Urco et al., 2019). Hardware and software details of both systems, i.e., SI-
112 MONe Peru and SIMONe Argentina, can be found in Chau et al. (2020).

113 SIMONe Argentina started operations by the end of September 2019 and has been
114 running since then with almost no interruptions. Figure 2 shows a summary of the de-
115 tection statistics for the first seven months of operations. The upper panel indicates the
116 normalized percentage of meteor counts for each individual link. The bottom panel is
117 used to present the average daily total counts for each month. Problems with the local
118 power supply at the transmitting site resulted in fewer meteor detections during April
119 of 2020. Besides, the receiving site at Gobernador Gregores was out of operation dur-

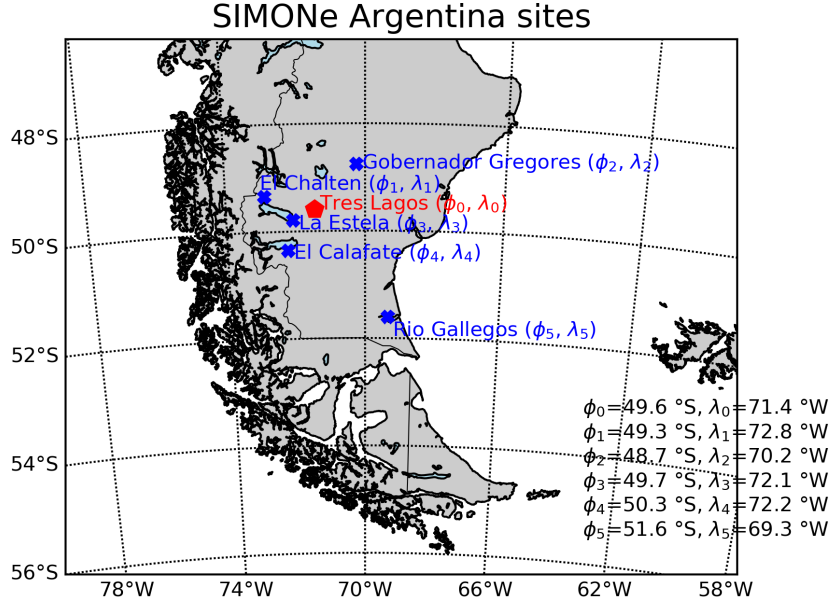


Figure 1. Map of SIMONE Argentina. The transmitter is indicated with a filled red pentagon, and the receivers are indicated with blue crosses.

120 ing December of 2019 due to damage in the antenna cables. Nevertheless, for most of
 121 the time, the number of counts was much higher than in standard specular meteor radars.
 122 The links concentrating most of the meteor detections are Tres Lagos-El Calafate and
 123 Tres Lagos-La Estela. Starting in March 2020, the link Tres Lagos-Rio Gallegos exhibits
 124 a considerable increase in the counts, as a result of having rotated the transmitting an-
 125 tennas by 90 degrees. By month, January presents the largest counts, with an average
 126 of more than 50000 meteor detections per day.

127 3 Data analysis

128 Specular meteor radars (SMRs) are used to measure the Doppler shift of meteor
 129 trails due to their drifting with the mesospheric neutral winds (e.g., Jones et al., 1998).
 130 In order to extract the wind information from the measurements, one may implement
 131 an all-sky fit of the Doppler velocities measured during a certain period of time and within
 132 a given altitude interval (e.g., Hocking et al., 2001; Holdsworth et al., 2004). In other
 133 words, one must solve the following equation:

$$\mathbf{u} \cdot \mathbf{k} = 2\pi f + \zeta, \quad (1)$$

134 where $\mathbf{u} = (u, v, w)$ is the neutral wind vector, with u , v and w being its zonal (east-
 135 west), meridional (north-south) and vertical (up-down) components, respectively. $\mathbf{k} =$
 136 (k_u, k_v, k_w) is the Bragg wave vector (scattered minus incident) in the meteor-centered
 137 east-north-up coordinate system (perpendicular to the meteor trail); f is the Doppler
 138 shift; and ζ is the Doppler shift uncertainty. For this equation to be valid, one must make
 139 the assumption that the winds at each given height interval are uniform during the se-
 140 lected period of time (homogeneous method). The results using the homogeneous method
 141 have been obtained assuming $w = 0$.

142 Monostatic SMRs commonly allow for hourly horizontal wind estimations every 2-
 143 3 km in altitude (e.g., Jacobi et al., 1999; Hoffmann et al., 2010). The wind estimates
 144 are representative of mean values over an area of ~ 200 km in radius. These horizon-

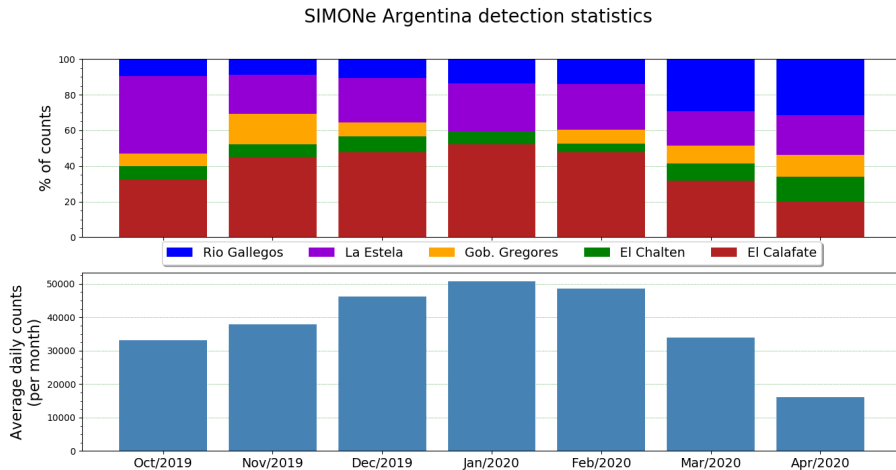


Figure 2. Upper panel: normalized percentage of meteor counts, color coded for each individual link. Bottom panel: monthly daily mean counts for all the links combined (see text for details).

145 tal winds can be further processed in order to obtain information about large scale waves
 146 such as planetary waves and tides (e.g., Murphy et al., 2006; Chau et al., 2015; Conte
 147 et al., 2018).

148 One of the advantages of using multistatic SMR networks is that the amount of
 149 meteor detections is significantly increased (e.g., Stober & Chau, 2015). During most of
 150 the time since it started operations, SIMONe Argentina has been capable of detecting
 151 more than 30000 meteors per day (see Figure 2). With such amounts of meteor detec-
 152 tions, one can not only reliably estimate horizontal winds with higher time and verti-
 153 cal resolutions (~ 15 min and 1 km, respectively), but also investigate second order pa-
 154 rameters such as the squares of the perturbation components of the radial velocities, i.e.,
 155 the momentum flux components (e.g., Spargo et al., 2019). Another advantage multi-
 156 static SMR networks present is that they are capable of sampling the observed volume
 157 from different viewing angles. In this scenario, the increased number of meteor detec-
 158 tions can be further exploited in order to estimate first-order derivatives of the horizon-
 159 tal winds, and in this way include in the estimation a mean vertical wind free of hori-
 160 zontal divergence contamination (e.g., Chau et al., 2017).

161 Below, we describe the main procedures used in this work, i.e., tidal estimation,
 162 wind estimation using a gradient method, and mean momentum flux estimation. For each
 163 of the three procedures, a first wind estimation is carried out in order to remove outliers.
 164 That is, Equation 1 is solved in bins of the same size as that used later on in each given
 165 procedure (e.g., 4 hour, 4 km in the gradient method); and then the radial velocities the
 166 values of which have a corresponding residual of more than 3 standard deviations are
 167 removed. This first wind estimation is carried out only in those bins containing a min-
 168 imum of 10 meteor detections.

169 3.1 Tidal estimation

170 Horizontal winds obtained from meteor radar measurements have been used for sev-
 171 eral decades to investigate tides and planetary waves in the MLT (e.g., Hocking & Thaya-
 172 paran, 1997; Fritts et al., 2012a). Different mathematical techniques such as least squares
 173 or wavelet analysis can be applied to the wind data in order to extract the tidal infor-

174 mation (e.g., Stening et al., 1997; Sandford et al., 2006; He et al., 2017). To avoid zero-
 175 padding or interpolating when encountering data gaps, a least squares approach was selected
 176 for this study.

177 After removing the outliers, Equation 1 was again fitted to the Doppler shift measure-
 178 ments. For this purpose, a weighted least squares (WLS) technique was implemented
 179 using bins of 1 hour and 2 km (in altitude), shifted by half an hour and 1 km, respec-
 180 tively. The inverse of the squared Doppler shift uncertainties (ζ in Eq. 1) were used as
 181 weights. The WLS was carried out only in those bins containing a minimum of 10 meteor
 182 detections. Then, under the assumption that the obtained hourly horizontal winds
 183 are the result of the superposition of a mean wind and different period oscillations, the
 184 following equation was fitted to the zonal (u) and meridional (v) wind components

$$[u + \psi_u, v + \psi_v] = [U_0, V_0] + \sum_{i=1}^4 [A_u, A_v]_i \cos\left(2\pi \frac{(t - [\phi_u, \phi_v]_i)}{T_i}\right). \quad (2)$$

185 Here, ψ_u and ψ_v are the Doppler shift uncertainties (error) propagated into the estimated
 186 winds; U_0 and V_0 are the mean zonal and meridional winds; A_{u_i} (A_{v_i}) and ϕ_{u_i} (ϕ_{v_i}) are
 187 the amplitude and phase, respectively, of the zonal (meridional) component of each con-
 188 sidered wave; $T_1 = 2$ day; T_i for $i > 1$ is the period of each considered tide ($T_2 = 24$
 189 h, $T_3 = 12$ h and $T_4 = 8$ h, for the diurnal, semidiurnal and terdiurnal solar tides, re-
 190 spectively); and t is the Universal Time (UT) in hours. The cosine of a sum was used
 191 to linearize Equation 2, which then was solved by applying the WLS method using a run-
 192 ning window of 4 days shifted by 1 day.

193 3.2 Wind field gradient method

194 If one relaxes the assumption of homogeneity, the wind field inside the observed
 195 area may be estimated using the gradient method. This method consists in approximat-
 196 ing the horizontal winds with their first-order Taylor expansion terms (e.g., Burnside et
 197 al., 1981; Browning & Wexler, 1968; Chau et al., 2017). This means introducing the fol-
 198 lowing expression into Equation 1

$$\mathbf{u}(x, y, z, t) = \mathbf{u}_0(z, t) + \mathbf{u}_x(z, t)(x - x_0) + \mathbf{u}_y(z, t)(y - y_0) + \mathbf{u}_z(z, t)(z - z_0), \quad (3)$$

199 where $\mathbf{u}_0 = (u_0, v_0, w_0)$ represents the mean wind; $\mathbf{x}_0 = (x_0, y_0, z_0)$ is a reference point;
 200 and

$$\begin{aligned} \mathbf{u}_x &= \left(\frac{du}{dx}, \frac{dv}{dx}, \frac{dw}{dx} \right) \\ \mathbf{u}_y &= \left(\frac{du}{dy}, \frac{dv}{dy}, \frac{dw}{dy} \right) \\ \mathbf{u}_z &= \left(\frac{du}{dz}, \frac{dv}{dz}, \frac{dw}{dz} \right). \end{aligned}$$

201 The mean wind and the first order derivatives depend only on time and height. The co-
 202 ordinates (x, y, z) are in km, and calculated taking into consideration the latitude, lon-
 203 gitude and altitude of each meteor detection and the radius of the Earth at the refer-
 204 ence point. \mathbf{x}_0 is determined using the latitude and longitude of the transmitting site,
 205 and the altitude of each height level considered in the WLS fit. The latter was imple-
 206 mented using bins of 4 hour and 4 km (in altitude), shifted by 15 minutes and 1 km, re-
 207 spectively. For this study, we have assumed that $(dw/dx, dw/dy, dw/dz) = \mathbf{0}$, which means
 208 solving for nine unknowns. In this method, a condition of having a minimum of forty
 209 meteor detections per bin was selected.

210 Mathematically speaking, the zero order approximation (\mathbf{u}_0) as well as the first order
 211 order derivatives (\mathbf{u}_x , \mathbf{u}_y and \mathbf{u}_z) are defined at the reference point, \mathbf{x}_0 . However, the de-
 212 pendence of our nine estimates on this reference point is not explicitly written in Equat-
 213 ion 3 for the following reason. The mean winds and the gradients are obtained after fit-
 214 ting measurements made at points randomly distributed within an area of roughly ~ 200

215 km of radius around \mathbf{x}_0 . Thus, it is assumed that they represent a “mean” zero order
 216 approximation, and “mean” first order derivatives, not only at the reference point, but
 217 over the whole area aforementioned.

218 3.3 Momentum flux estimates

219 The procedure followed in this study to estimate the GW momentum flux is based
 220 on the works by Thorsen et al. (1997) and Hocking (2005). It consists in applying a least
 221 square method to solve the following equation

$$(\mathbf{u}' \cdot \mathbf{k})^2 = (2\pi(f - \hat{f}))^2. \quad (4)$$

222 In this expression, \mathbf{k} and f are, respectively, the same Bragg wave vector and same Doppler
 223 shift as in Equation 1, but \mathbf{u}' represents the perturbed wind vector instead. \hat{f} is a so-
 224 called mean Doppler shift,

$$\hat{f} = \mathbf{u} \cdot \mathbf{k} / 2\pi, \quad (5)$$

225 where \mathbf{u} is the mean wind that results from solving Equation 1 or 3. To guarantee more
 226 reliable values of the six unknowns ($\langle u'u' \rangle$, $\langle v'v' \rangle$, $\langle u'w' \rangle$, $\langle v'w' \rangle$, $\langle u'v' \rangle$ and $\langle w'w' \rangle$),
 227 the fit was performed only in those bins containing forty meteor detections or more.

228 From Equations 4 and 5, it follows that different momentum flux estimates may
 229 be obtained depending on the mean wind that is used to determine \hat{f} . In this study, the
 230 wind estimates that result from applying the gradient method were used to calculate \hat{f}
 231 (see previous section). That is, Equation 3 (with $dw/dx = dw/dy = dw/dz = 0$) was
 232 introduced into Equation 1, and the latter then solved using bins of 4 hour and 8 km,
 233 shifted by 15 min in time and 1 km in altitude. Finally, Equation 4 was solved in bins
 234 of 4 hour and 4 km (in altitude), shifted by 30 min and 1 km, respectively.

235 4 Results and discussion

236 One of the main goals of this work is to provide, for the first time, information on
 237 the MLT dynamics over southern Patagonia obtained using SIMONe Argentina. For this
 238 reason, our results are discussed as they are presented.

239 4.1 Mean winds and tides

240 In Figure 3, we present the mean zonal (U_0) and meridional (V_0) winds, and the
 241 total amplitudes of the quasi two-day planetary wave (Q2DW) and the diurnal (D1), semidi-
 242 urnal (S2) and terdiurnal (T3) solar tides. The vertical black dashed line indicates Jan-
 243 uary 1st 2020. The term *total amplitude* refers to the magnitude of the vector sum of
 244 the corresponding zonal and meridional components of each fitted wave. The statisti-
 245 cal uncertainties of the estimated parameters are shown in the right column panels. All
 246 quantities were obtained after applying the procedure detailed in Section 3.1. Data gaps
 247 are shown in white.

248 From inspection of Figure 3, two features stand out: the S2 tide is the dominant
 249 wave, with amplitudes in the order of 40-65 m/s, and the Q2DW exhibits strong enhance-
 250 ments after 4 January 2020. It is well known that the semidiurnal solar tide at middle
 251 latitudes dominates over all other tidal components (e.g., Andrews et al., 1987; Pancheva
 252 & Mukhtarov, 2011). Furthermore, many studies of tides in the northern hemisphere have
 253 reported that S2 decreases significantly around the onset of a sudden stratospheric warm-
 254 ing (SSW) event, to later on recover and reach even larger amplitudes than those exhib-
 255 ited prior to the SSW (e.g., Chau et al., 2015; Siddiqui et al., 2018; Conte et al., 2019).
 256 In September of 2019, approximately 12 days before the 27th (first day of available data
 257 from SIMONe Argentina), a SSW event was registered in the southern hemisphere (e.g.,

258 Yamazaki et al., 2020). Interestingly enough, the largest amplitudes of S2 are seen be-
 259 tween 27 September and 12 October, which may be an indicative of the recovery phase
 260 of S2 after the weakening associated with a SSW event. On the other hand, it is also pos-
 261 sible that the reported enhancement of S2 is simply the result of changes in the prop-
 262 agation conditions of this tidal component. For example, the S2 amplitudes may change
 263 due to different responses of the symmetric and antisymmetric Hough modes to the weaker
 264 and more hemispherically symmetric mean zonal wind typical of the equinox times. Pre-
 265 vious studies of the S2 tide at middle latitudes of the southern hemisphere have shown
 266 a decrease of S2 in the beginning of September, and a later recovery by the beginning
 267 of October (e.g., Conte et al., 2017). However, this decrease/increase behavior of S2 dur-
 268 ing the September-October months is not obvious every year. Lastly, note that for the
 269 entire dataset analyzed in this study, S2 presents significant intraseasonal variability, which
 270 becomes evident in the many, although weaker, enhancements observed after ~ 31 Oc-
 271 tober.

272 The Q2DW at middle latitudes has been reported to reach maximum amplitudes
 273 during the summer (e.g., Kumar et al., 2018). In our results, the Q2DW is active mostly
 274 in summer, in agreement with previous studies. Even more, it becomes the dominant wave
 275 by the end of January 2020, with amplitudes larger than those corresponding to S2. Offermann
 276 et al. (2011) showed that the Q2DW exhibits a triple peak structure in the NH during
 277 summer. Although it may not be obvious at first, after a more through inspection of Fig-
 278 ure 3, it can be noticed that the largest amplitudes of the Q2DW are distributed in three
 279 subsequent enhancements, around 7, 13 and 19 January. A fourth enhancement can be
 280 seen around 9 February, but the latter is significantly weaker than the previous three.

281 Both the diurnal and terdiurnal solar tides exhibit considerable intraseasonal vari-
 282 ability. In the case of D1, its activity becomes more evident mostly below ~ 90 km and
 283 during summer. Above ~ 92 km, and mainly during equinox times, T3 becomes more
 284 noticeable, with amplitudes similar to those corresponding to D1.

285 Compared to five-year average values at 54° S presented by Conte et al. (2017), the
 286 summer reversal of the mean zonal wind shown in Figure 3 is observed at altitudes ap-
 287 proximately two km lower. This is consistent with previous studies reporting a decrease
 288 with latitude of the height of the zonal wind summer reversal (e.g., Hoffmann et al., 2010;
 289 Wilhelm et al., 2019). Besides, it might seem that U_0 starts the transition into summer
 290 conditions relatively early, around 3 October. However, above ~ 92 km, U_0 experiences
 291 a late reversal to westward conditions around 24 October, to finally go into summer con-
 292 ditions (i.e., eastward above the mesopause) about five days later. V_0 blows mainly to-
 293 wards the equator, and only after 10 March poleward values start to dominate.

294 The statistical uncertainties of all the fitted parameters presented in Figure 3 are
 295 very small. Only above 103 km and below 77 km, values of ~ 2 -3 m/s are obtained (not
 296 shown). The low statistical uncertainties are a consequence of the large amount of me-
 297 teor detections provided by SIMONE Argentina. By solving Equation 1 in bins of one
 298 hour and two km, one guarantees wind estimates with very low uncertainties. The lat-
 299 ter, combined with the fact the WLS method used to solve Equation 2 is applied to a
 300 very well conditioned matrix, results in small statistical uncertainties.

301 4.2 Gradients and vertical wind

302 In Figure 4, we present one week of 4-hour, 4-km mean winds and gradients ob-
 303 tained after applying the procedure described in Section 3.2. The first row shows, from
 304 left to right, the mean zonal (u_0), meridional (v_0) and vertical (w_0) winds. The panels
 305 in the middle row are used to show the zonal eastward, northward and upward (first or-
 306 der) derivatives, i.e., u_x , u_y and u_z , respectively. The bottom row shows the same as the
 307 middle one, but for the meridional component, i.e., v_x , v_y and v_z . The mean winds are
 308 given in m/s, and the gradients in m/s/km. The mean vertical wind and the gradients

SIMONe Argentina - Mean winds & tides

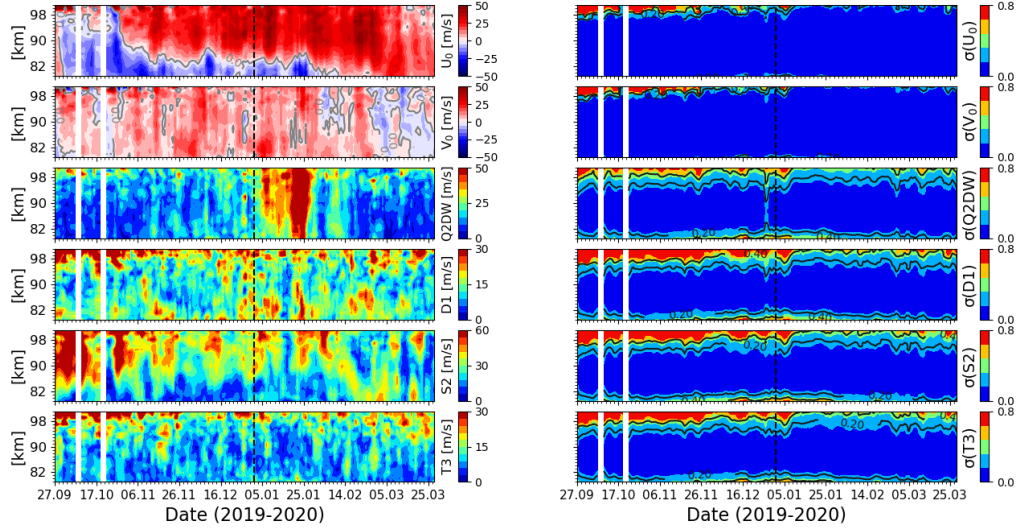


Figure 3. Mean zonal (U_0) and meridional (V_0) winds, the quasi two-day planetary wave (Q2DW), and the diurnal (D1), semidiurnal (S2) and terdiurnal (T3) solar tides during September 2019 - April 2020 over SIMONe Argentina. The corresponding statistical uncertainties (in m/s) are shown in the right column. All parameters were estimated using a four-day running window shifted by one day. The vertical black dashed line indicates January 1st 2020.

309 are shown only between 80 and 97 km of altitude, where the data coverage is good enough
 310 to estimate them more reliably.

311 Before starting the description of the main features observed in Figure 4, it is im-
 312 portant to stress here that the variability seen in the mean winds is representative of large
 313 scale structures, with periods greater than four hours and vertical wavelengths larger than
 314 four km. Both u_0 and v_0 exhibit a clear diurnal and semidiurnal periodicity, the latter
 315 being more evident, something expected given the latitude of SIMONe Argentina. The
 316 semidiurnal periodicity is also very clear in the vertical gradients, u_z and v_z , which in-
 317 dicates a strong influence of the S2 tide in the vertical changes of the horizontal winds.
 318 Although they may not be evident in Figure 4, other periodicities are present in the ver-
 319 tical gradients. For example, GW effects can be noticed below 90 km. At these altitudes,
 320 u_z is mainly positive (with mean values in the order of 20 m/s/km). In fact, during most
 321 of the summertime, below ~ 90 km of altitude, and when averaged over longer periods
 322 of time, e.g., 1 day, u_z is strongly dominated by positive amplitudes (not shown here).
 323 During the summer, westward zonal winds are dominant in the stratosphere and meso-
 324 sphere. This condition allows eastward propagating GWs to easily reach mesospheric al-
 325 titudes, where they break and deposit momentum and energy. This deposition of mo-
 326 mentum creates an eastward drag that decelerates the zonal (westward) wind. Due to
 327 the Coriolis effect, the deceleration of the zonal wind introduces an equatorward merid-
 328 ional wind component, which in turn leads to an upward motion and a subsequent (adi-
 329 abatic) cooling of the mesopause region (e.g., Smith, 2012). Finally, due to the thermal
 330 wind equation, $u_z \approx -\alpha(\phi)\partial T/\partial y$ (where y is positive towards north, T is the temper-
 331 ature, and α is a factor that depends on the sine of the latitude, ϕ), the adiabatic cool-
 332 ing results in the positive values of u_z . In the case of v_z , the amplitudes are in the or-
 333 der of 3-5 m/s/km weaker than those of u_z , but the semidiurnal periodicity is seen at

334 all altitudes. No evident pattern or structure in time can be noticed when v_z is averaged
 335 over longer periods of time.

336 In the case of u_x and v_x , amplitude values are in the order of 0.1-0.3 m/s/km. The
 337 larger amplitudes of u_y (compared to u_x) may be an indicative of zonal wind latitudi-
 338 nal changes related to the Antarctic polar vortex, part of which usually locates below
 339 the region seen by SIMONe Argentina (e.g., Figure 8 in Orte et al. (2019)). The upward
 340 component of the relative vorticity can be coarsely approximated by $v_x - u_y$ (for a pre-
 341 cise calculation, one needs to include the latitude information; see Equation A16 in Chau
 342 et al. (2017)). Below ~ 84 km, $v_x - u_y$ values are mainly positive, which suggests coun-
 343 ter-clockwise vortical effects. Besides, differences between the amplitudes of u_y , v_x and
 344 u_x , v_y , suggest that changes in the horizontal gradients due to GWs depend on the prop-
 345 agation direction of the these waves.

346 The errors in both the horizontal and vertical gradients are in the order of 5-10 %.
 347 For example, for the week of data shown in Figure 4, the root mean square errors of u_x ,
 348 u_y , u_z , v_x , v_y , and v_z are 0.011, 0.023, 1.1, 0.022, 0.013, and 0.99 m/s/km, respectively.

349 Previous observational studies have investigated the horizontal gradients in the zonal
 350 and meridional winds (e.g., Conde & Smith, 1998; Meriwether et al., 2008; Chau et al.,
 351 2017). However, the present study is the first one to show results on both the horizon-
 352 tal and vertical gradients of MLT horizontal winds over southern Patagonia. Chau et
 353 al. (2017) showed that horizontal divergence values of ~ 0.1 m/s/km are large enough
 354 to introduce a mean apparent vertical wind of 1-2 m/s. After calculating $u_x + v_y$, one
 355 obtains values in the order of 0.4-0.5 m/s/km. Consequently, one can now understand
 356 the importance of estimating the vertical wind together with the gradients. By doing so,
 357 one eliminates the effects of biases introduced in w_0 by the mean horizontal variability
 358 of u and v . However, the horizontal variability within scales smaller than the observed
 359 volume is not removed, and will affect the vertical wind estimates.

360 The four-hour mean vertical winds (w_0) exhibit large amplitudes and considerable
 361 variability both in time and height. The errors in these estimates are in the order of 1-
 362 2 m/s. After computing daily averages, vertical wind amplitudes are reduced to a few
 363 m/s, which are still considerably large values. Previous studies have investigated MLT
 364 mean vertical winds using specular meteor radars. For example, Babu et al. (2012) and
 365 Egito et al. (2016) reported that the vertical winds at low latitudes may reach magni-
 366 tudes of 6-10 m/s. Using VHF radar measurements, Fritts et al. (1990) observed that
 367 at summer mesopause altitudes vertical velocities may reach values of up to 10 m/s, but
 368 within time scales of 5-30 minutes. That is, vertical winds should exhibit values in the
 369 order of a few to tens cm/s when averaged over periods of 1 day or more (e.g., Lu et al.,
 370 2017).

371 There are several factors that adversely affect our vertical wind estimates. (1) The
 372 daily variability in the meteor counts (meteor detections maximize early in the morn-
 373 ing and minimize in the evening) can result in irregular time sampling at altitudes where
 374 the detections are lower, i.e., above 97 km and below 80 km, in the case of SIMONe Ar-
 375 gentina. For this reason, we have limited our analysis of w_0 to altitudes between 80 and
 376 97 km. (2) Despite the multistatic configuration, sometimes the meteor detections are
 377 not well distributed among all five links. This affects in a similar way every altitude ob-
 378 served by SIMONe Argentina. (3) Small-scale horizontal variability is not removed af-
 379 ter applying the gradient method. Hence, horizontal changes of the zonal and meridional
 380 winds occurring within the observed volume can easily leak into the vertical winds, and
 381 thus result in the large w_0 values presented in Figure 4. To better understand and quan-
 382 tify the adverse impact of points (2) and (3), we are currently working in applying the
 383 gradient method to forward modelled data using different geometric configurations. This
 384 will shed light on the reliability of the vertical winds presented in this study as well as
 385 other studies using multistatic SMR configurations.

(4h, 4km) mean winds and gradients over SIMONe Argentina

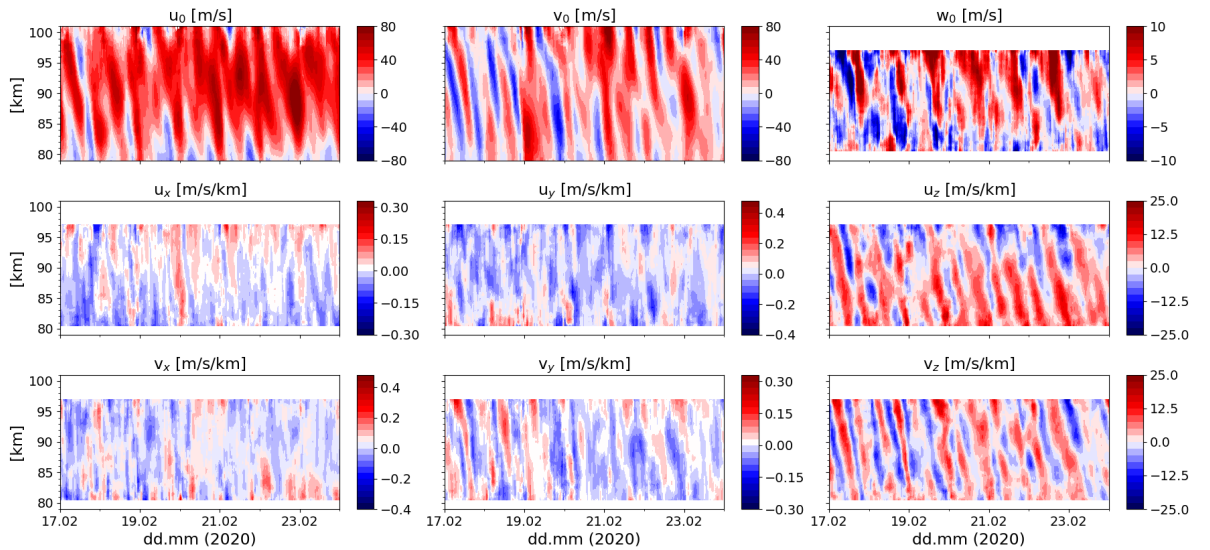


Figure 4. SIMONe Argentina estimates of: (first row) mean zonal (u_0), meridional (v_0) and vertical (w_0) winds; (second row) zonal eastward (u_x), meridional (u_y) and upward (u_z) derivatives; (third row) meridional eastward (v_x), northward (v_y) and upward (v_z) derivatives. All parameters were estimated using a 4 hour, 4 km (in vertical) bin, shifted by 15 min and 1 km, respectively.

386 Despite the large amplitudes, coherent phase structures can be seen in w_0 . For ex-
 387 ample, around 17 February one can observe a clear diurnal periodicity. Diurnal wave sig-
 388 natures in w_0 have been found throughout the entire SIMONe Argentina dataset (not
 389 shown). Moreover, similar features have been observed in the mean vertical winds over
 390 Peru and northern Germany (Chau et al., 2020; Charuvil Asokan et al., 2020). Hence,
 391 it is possible that our results on w_0 are also revealing real geophysical features, e.g., di-
 392 urnal tidal effects. This will be carefully investigated in future studies.

393 4.3 Gravity-wave-driven momentum flux

394 We now present and discuss the momentum flux estimates obtained after subtract-
 395 ing the mean winds calculated following the gradient method, i.e., the u_0 , v_0 and w_0 that
 396 were estimated together with the gradients. In Figure 4, it can be seen that the hori-
 397 zontal wind gradients and the vertical mean wind exhibit considerable variability, both
 398 in time and altitude. Part of this variability is leaked into the mean horizontal winds when
 399 one solves Equation 1 without including the gradients and w_0 in the wind vector \mathbf{u} . This
 400 implies that the u_0 and v_0 obtained using the gradient method constitute a better rep-
 401 resentation of the real mean wind, provided that enough meteors are detected in order
 402 to accomplish a robust wind estimation. Besides, it is important to have in mind that
 403 the subtracted winds were estimated in bins of 4 hour and 8 km (in altitude). This means
 404 that the corresponding momentum flux estimates are representative mostly of waves with
 405 temporal and vertical scales of less than 4 hour and 8 km, respectively.

406 In Figure 5, we present 28-day averages of the momentum flux estimates that re-
 407 sult from subtracting the \hat{f} that was calculated using the u_0 , v_0 , w_0 mentioned in the
 408 previous paragraph (see Equation 4). The averages were calculated over 28 days in or-

409 der to obtain estimates that are statistically more significant. The upper panels present
 410 U and V , which correspond to the 28-day averages of the mean zonal and meridional winds,
 411 respectively. The middle panels are used to show the 28-day mean horizontal momen-
 412 tum vertical fluxes, $\langle u'w' \rangle$, $\langle v'w' \rangle$. The statistical uncertainties of $\langle u'w' \rangle$ and $\langle v'w' \rangle$,
 413 i.e., $\sigma(u'w')$ and $\sigma(v'w')$, respectively, are shown in the bottom panels.

414 Momentum flux estimations based on SMR observations were first presented by Hocking
 415 (2005). Since then, several studies have investigated momentum fluxes using meteor radar
 416 winds (e.g., Fritts et al., 2010; Placke et al., 2011b; Fritts et al., 2012b; Andrioli et al.,
 417 2013; Placke et al., 2015, and references therein). More recently, de Wit et al. (2016) ob-
 418 served a modulation by the quasi-biennial oscillation (QBO) of the momentum fluxes
 419 over Tierra del Fuego, an island south of Santa Cruz province. Typical amplitudes of $\langle u'w' \rangle$
 420 and $\langle v'w' \rangle$ reported in these previous studies rarely reach values larger than 60-70 m^2/s^2 .
 421 Using a multistatic meteor radar network over southern Australia, Spargo et al. (2019)
 422 observed values for $\langle u'w' \rangle$ and $\langle v'w' \rangle$ in the order of 40-60 m^2/s^2 , which are larger
 423 than momentum flux absolute values obtained from satellite measurements (e.g., Ern et
 424 al., 2011; Trinh et al., 2018). The latter is most likely due to observational filtering in-
 425 herent to satellites.

426 From Figure 5, it can be seen that our momentum flux estimates have amplitudes
 427 in the order of 25-45 m^2/s^2 . Some large amplitudes of about 90 m^2/s^2 can be observed
 428 above 96 km of altitude, where the corresponding statistical uncertainties are in the or-
 429 der of 10 % or more (see bottom panels). Both momentum flux estimates exhibit vari-
 430 ability in time and height, although it is more evident in the case of $\langle u'w' \rangle$. Notice that
 431 despite the 28-day averaging, the magnitudes of $\langle u'w' \rangle$ and $\langle v'w' \rangle$ are considerable
 432 throughout the entire period of time analyzed in this study. Momentum flux estimates
 433 averaged over 20 days presented by Placke et al. (2015) exhibit maximum amplitudes
 434 of 6-8 m^2/s^2 during the summer of the northern hemisphere. The largest amplitudes of
 435 ten-day momentum flux estimates shown by Spargo et al. (2019) reach values of 30-40
 436 m^2/s^2 in the beginning of the spring of the southern hemisphere. On the other hand, de
 437 Wit et al. (2017) observed monthly mean momentum fluxes over Tierra del Fuego with
 438 amplitudes larger than 70 m^2/s^2 during the summer. These amplitude values are in the
 439 same order as those obtained in our study. Hence, it is clear that the wave activity in
 440 the MLT region over the Patagonian sector is very strong. This is also consistent with
 441 previous studies based on satellite measurements (e.g., Ern et al., 2011), and numerical
 442 simulations (e.g., Lund et al., 2020).

443 As GWs propagate upwards, they transfer momentum and energy into the mean
 444 flow. Consequently, a decrease in the vertical flux of zonal momentum should correspond
 445 with an increase in the zonal wind speed (e.g., Fan et al., 1991). In other words, a de-
 446 crease of the momentum flux indicates that a wave drag has been introduced into the
 447 mean flow, thus triggering an acceleration of the zonal wind. Our results are consistent
 448 with this reasoning, since for altitudes below 90-92 km, $\langle u'w' \rangle$ amplitudes, which are
 449 mostly positive, exhibit a clear vertical gradient: as the altitude increases, they progres-
 450 sively decrease from values of around 70-75 m^2/s^2 below 82 km, to values of $\sim 10 \text{ m}^2/\text{s}^2$
 451 above 90 km. The latter is also consistent with the results on u_z presented in the pre-
 452 vious section. Besides, note that after 22 February, negative values of $\langle u'w' \rangle$ start to
 453 develop below 90-91 km. At that time of the year, U has become eastward at all alti-
 454 tudes observed by SIMONe, a condition that allows westward propagating GWs to reach
 455 higher altitudes and, most likely, induce the aforementioned $\langle u'w' \rangle$ negative values.

456 In the case of $\langle v'w' \rangle$, an upward movement of southward momentum dominates
 457 mostly below ~ 91 km, from the beginning of October until the end of March. During
 458 the last week of December 2019, positive values of $\langle v'w' \rangle$ start to dominate above 92-
 459 94 km, an altitude range that had been dominated by negative values of $\langle v'w' \rangle$ since
 460 the beginning of November 2019. During the latter, and approximately above 96 km of
 461 altitude, an upward movement of eastward momentum can be noticed again. These pos-

462 itive values of $\langle u'w' \rangle$ develop very abruptly around 26 November, and remain domi-
 463 nant above 96 km for more than 25 days. We wonder if this might be an indicative of
 464 eastward momentum deposition by GWs that were in-situ generated at altitudes above
 465 90 km.

466 Momentum flux estimates obtained after subtracting the mean winds determined
 467 with the homogeneous method were also analyzed (not shown). In this case, only the
 468 4-hour, 8-km mean horizontal winds are used to determine \hat{f} (see Equation 5). These
 469 momentum flux estimates have similar amplitudes to those presented in Figure 5. How-
 470 ever, they exhibit some differences in their variability in time and altitude, and their sta-
 471 tistical uncertainties are larger than those shown in Figure 5. It is for the latter and for
 472 consistency reasons, that the present study has been focused on analyzing the momen-
 473 tum fluxes that result from subtracting the mean horizontal and vertical winds obtained
 474 after applying the gradient method.

475 To finalize, we discuss the procedure followed to estimate $\sigma(u'w')$ and $\sigma(v'w')$, and
 476 the reason for calculating 28-day averages. Unless one knows with some degree of cer-
 477 tainty that a given wave event has occurred, the effects of GWs should be treated as stochas-
 478 tic processes. In other words, the mean momentum flux estimates are highly dependent
 479 on the effects of geophysical variability. Kudeki and Franke (1998) showed that in or-
 480 der to obtain statistically significant momentum flux estimates at mesospheric heights,
 481 one must consider averaging intervals of more than 25 days. Specifically, they found that
 482 the statistical uncertainty of $\langle u'w' \rangle$ can be approximated with:

$$\sigma(u'w') = \sqrt{\frac{\langle u'u' \rangle \langle w'w' \rangle}{T/\tau}}, \quad (6)$$

483 where, $\langle u'u' \rangle$ and $\langle w'w' \rangle$ are averaged over the interval of time T ; and τ is equal to
 484 half of the mesosphere Brunt-Väisälä period (~ 7 min). $\sigma(v'w')$ is obtained using same
 485 Equation 6, but replacing $\langle u'u' \rangle$ by $\langle v'v' \rangle$. Selection of an averaging window $T =$
 486 28 days resulted in the values presented in Figure 5. In this way, the $\langle u'w' \rangle$ and $\langle v'w' \rangle$
 487 obtained from our study must be understood as representatives of a monthly mean mo-
 488 mentum flux due to waves with periods of 4 h or less, and horizontal scales less than 400
 489 km. Besides, for those estimates corresponding to altitudes lower than ~ 98 km, statisti-
 490 cal uncertainties between 2 and 15-16 m^2/s^2 should be taken into consideration.

491 The momentum flux estimates are also affected by the correlated Doppler shift er-
 492 rors. In other words, because the Doppler shift uncertainties are squared when introduced
 493 into Equation 4, the resulting momentum flux estimates are in fact an overestimation
 494 of the real $\langle u'w' \rangle$ and $\langle v'w' \rangle$ (Vierinen et al., 2019). However, given that the error
 495 propagated Doppler shift uncertainties we obtained are small (\sim one order of magnitude
 496 smaller than the statistical uncertainties) and that the amplitudes of $\langle u'w' \rangle$ and $\langle v'w' \rangle$
 497 are large, the effects of the correlated errors were neglected in this study. We plan to fur-
 498 ther investigate this issue by extending our analysis to include non-zero lag second-order
 499 statistics of the wind velocities.

500 5 Concluding remarks

501 The first multistatic meteor radar based studies of mean winds, tides, gradients and
 502 momentum flux over the southern part of Patagonia have been presented in this paper.
 503 By doing this, we have demonstrated the ability of SIMONe Argentina to obtain not only
 504 information on typical MLT parameters such as mean winds and tides, but also to suc-
 505 cessfully estimate previously little investigated parameters, such as horizontal and ver-
 506 tical gradients of the horizontal winds. Using the latter, one can estimate, e.g., the hor-
 507 izontal divergence and the relative vorticity, parameters from which global circulation
 508 models can benefit and in this way help to further the understanding of MLT dynam-
 509 ics.

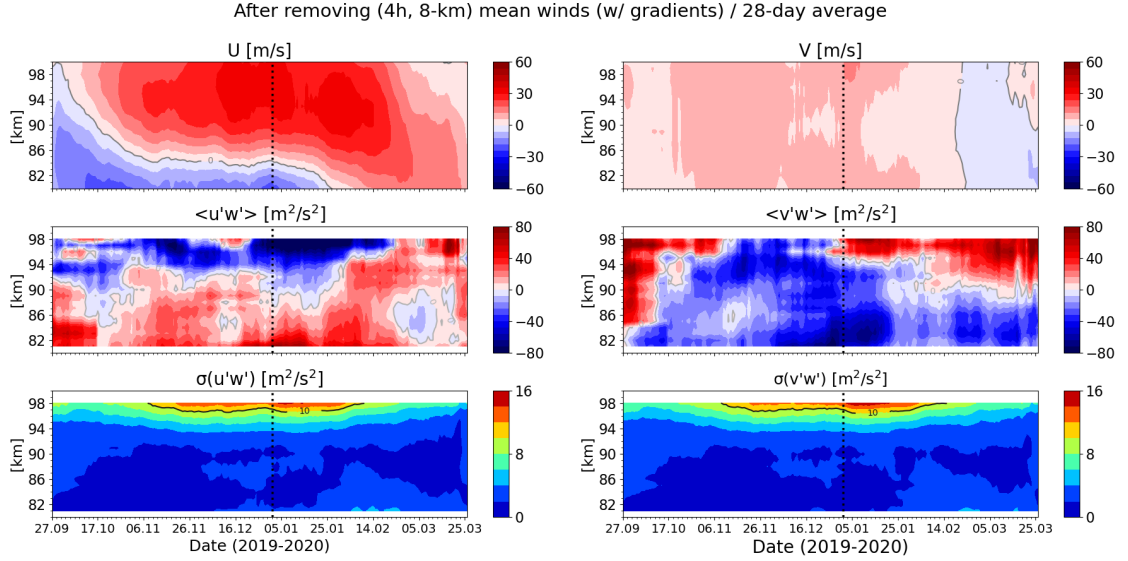


Figure 5. 28-day averages of 4-h, 8-km mean zonal and meridional winds (U and V , respectively), horizontal momentum vertical fluxes ($\langle u'w' \rangle$, $\langle v'w' \rangle$) and their corresponding statistical uncertainties ($\sigma(u'w')$, $\sigma(v'w')$). 4 hour, 8 km (in altitude) mean horizontal and vertical winds estimated in combination with the gradients (i.e., the u_0 , v_0 , w_0 described in Section 3.2) were subtracted before estimating the momentum flux. The vertical black dashed line indicates 1 January 2020.

510 Our results show a strong positive vertical gradient in the zonal wind during the
 511 summer, in agreement with the residual mean meridional circulation. Besides, the north-
 512 ward zonal gradient (u_y) is stronger than the eastward zonal gradient (u_x), which indi-
 513 cates latitudinal changes of the zonal wind most likely due to the influence of the south-
 514 ern hemisphere polar vortex. Mean vertical winds (w_0) have also been estimated, but
 515 only when the horizontal and vertical gradients were taken into account.

516 Momentum fluxes, $\langle u'w' \rangle$ and $\langle v'w' \rangle$, have been estimated after removal of hor-
 517 izontal and vertical mean winds that were fitted together with the horizontal wind gra-
 518 dients. Compared to some previous studies, our momentum flux estimates exhibit larger
 519 amplitudes, which indicates that the GW activity in the MLT over southern Patagonia
 520 is very strong. The statistical uncertainties of $\langle u'w' \rangle$ and $\langle v'w' \rangle$ were also included
 521 in the analysis. The latter revealed that in order to have statistically significant momen-
 522 tum flux estimates, one should consider averages of at least 28 days. In this way, our re-
 523 sults must be considered as representative of monthly mean momentum fluxes, driven
 524 by waves with periods shorter than 4 hours, vertical wavelengths shorter than 8 km, and
 525 horizontal scales less than 400 km.

526 We are confident that SIMONE Argentina has also the potential to investigate non-
 527 zero lag second-order statistics of MLT wind velocities, e.g., by using correlation func-
 528 tion techniques such as those presented in Vierinen et al. (2019). This will be explored
 529 in future studies. Besides, we also plan to investigate momentum flux estimates with-
 530 out averaging over long periods of time, provided there is evidence of specific (determi-
 531 nistic) wave events occurring in the troposphere/stratosphere.

532 **Acknowledgments**

533 We deeply thank Nico Pfeffer, Matthias Clahsen, Jens Wedrich and Thomas Barth
 534 (at IAP) for their invaluable help and expertise during the installation of SIMONe Ar-
 535 gentina; and Jonathan Quiroga and Nahuel Díaz (CONICET) for helping with the lo-
 536 gistics prior to the installation. We would also like to thank Darío Godoy and Facundo
 537 Olivares (at Tres Lagos); Pablo Quiroz (at La Estela); Martín “el griego” Palopoli and
 538 National Parks staff (at El Chaltén); the Consejo Agrario de la Provincia de Santa Cruz
 539 (at Gob. Gregores and El Calafate); and the BAM-GAL (Argentina Air Force) for their
 540 support and help in maintaining the sites.

541 We thank Dr. Xinzhao Chu for her useful and constructive comments, which have
 542 helped us to improve our work.

543 This work was partially supported by the Deutsche Forschungsgemeinschaft (DFG,
 544 German Research Foundation) under SPP 1788 (DynamicEarth) CH 1482/2 (DYNA-
 545 MITE2), and by the Bundesministerium für Bildung und Forschung via project WASCLIM-
 546 IAP part of the ROMIC-II program.

547 The data used to produce the figures is available in HDF5 format at DOI: 10.22000/342.

548 **References**

- 549 Andrews, D. G., Holton, J. R., & Leovy, C. B. (1987). Middle atmosphere dynamics.
 550 *Academic Press, San Diego, California*. doi: 10.1002/qj.49711548612
- 551 Andrioli, V. F., Batista, P. P., Clemesha, B. R., Schuch, N. J., & Buriti, R. A.
 552 (2015). Multi-year observations of gravity wave momentum fluxes at low and
 553 middle latitudes inferred by all-sky meteor radar. *Ann. Geophys.*, *33*, 1183–
 554 1193. doi: 10.5194/angeo-33-1183-2015
- 555 Andrioli, V. F., Fritts, D. C., Batista, P. P., & Clemesha, B. R. (2013). Im-
 556 proved analysis of all-sky meteor radar measurements of gravity wave
 557 variances and momentum fluxes. *Ann. Geophys.*, *31*, 889–908. doi:
 558 10.5194/angeo-31-889-2013
- 559 Babu, V. S., Ramkumar, G., & John, S. R. (2012). Seasonal variation of plan-
 560 etary wave momentum flux and the forcing towards mean flow accelera-
 561 tion in the MLT region. *J. Atmos. Sol. Terr. Phys.*, *78-79*, 53–61. doi:
 562 10.1016/j.jastp.2011.05.010
- 563 Browning, K. A., & Wexler, R. (1968). The determination of kinematic properties of
 564 a wind field using Doppler radar. *J. Appl. Meteorol.*, *7*(1), 105–113.
- 565 Burnside, R. G., Herrero, F. A., Meriwether, J. W., & Walker, J. C. G. (1981). Op-
 566 tical observations of thermospheric dynamics at Arecibo. *J. Geophys. Res.*, *86*,
 567 5532–5540.
- 568 Charuvil Asokan, H., Chau, J. L., Marino, R., Vierinen, J., Vargas, F., Urco, J. M.,
 569 ... Jacobi, C. (2020). Study of second-order wind statistics in the meso-
 570 sphere and lower thermosphere region from multistatic specular meteor radar
 571 observations during the SIMONe 2018 campaign. *Atmos. Chem. Phys.* doi:
 572 10.5194/acp-2020-974
- 573 Chau, J. L., Hoffmann, P., Pedatella, N. M., Matthias, V., & Stober, G. (2015).
 574 Upper mesospheric lunar tides over middle and high latitudes during sudden
 575 stratospheric warming events. *J. Geophys. Res.: Space Phys.*, *120*(4), 3084–
 576 3096. doi: 10.1002/2015JA020998
- 577 Chau, J. L., Stober, G., Hall, C. M., Tsutsumi, M., Laskar, F. I., & Hoffmann, P.
 578 (2017). Polar mesospheric horizontal divergence and relative vorticity measure-
 579 ments using multiple specular meteor radars. *Radio Sci.*, *52*, 811–828. doi:
 580 10.1002/2016RS006225
- 581 Chau, J. L., Urco, J. M., Vierinen, J., Harding, B. J., Clahsen, M., Pfeffer, N.,

- 582 ... Erickson, P. J. (2020). Multistatic specular meteor radar network in
 583 Peru: System description and initial results. *Earth and Space Science*. doi:
 584 doi.org/10.1002/essoar.10503328.1
- 585 Chau, J. L., Urco, J. M., Vierinen, J. P., Volz, R. A., Clahsen, M., Pfeffer, N.,
 586 & Trautner, J. (2019). Novel specular meteor radar systems using co-
 587 herent MIMO techniques to study the mesosphere and lower thermo-
 588 sphere. *Atmospheric Measurement Techniques*, *12*(4), 2113–2127. doi:
 589 10.5194/amt-12-2113-2019
- 590 Clemesha, B. R., Batista, P. P., Buriti da Costa, R. A., & Schuch, N. (2009). Sea-
 591 sonal variations in gravity wave activity at three locations in Brazil. *Ann. Geo-*
 592 *phys.*, *27*, 1059–1065. doi: 10.5194/angeo-27-1059-2009
- 593 Conde, M., & Smith, R. W. (1998). Spatial structure in the thermospheric horizon-
 594 tal wind above Poker Flat, Alaska, during solar minimum. *J. Geophys. Res.*,
 595 *103*, 9449–9472. doi: 10.1029/97JA03331
- 596 Conte, J. F., Chau, J. L., Laskar, F. I., Stober, G., Schmidt, H., & Brown, P.
 597 (2018). Semidiurnal solar tide differences between fall and spring transi-
 598 tion times in the Northern Hemisphere. *Ann. Geophys.*, *36*, 999–1008. doi:
 599 10.5194/angeo-36-999-2018
- 600 Conte, J. F., Chau, J. L., & Peters, D. H. W. (2019). Middle- and high-latitude
 601 mesosphere and lower thermosphere mean winds and tides in response to
 602 strong polar-night jet oscillations. *J. Geophys. Res.*, *124*, 9262–9276. doi:
 603 10.1029/2019JD030828
- 604 Conte, J. F., Chau, J. L., Stober, G., Pedatella, N., Maute, A., Hoffmann, P., ...
 605 Murphy, D. J. (2017). Climatology of semidiurnal lunar and solar tides at
 606 middle and high latitudes: Interhemispheric comparison. *J. Geophys. Res.*,
 607 *122*. doi: 10.1002/2017JA024396
- 608 de Wit, R. J., Janches, D., Fritts, D. C., & Hibbins, R. E. (2016). QBO modu-
 609 lation of the mesopause gravity wave momentum flux over Tierra del Fuego.
 610 *Geophys. Res. Lett.*, *43*, 4049–4055. doi: 10.1002/2016GL068599
- 611 de Wit, R. J., Janches, D., Fritts, D. C., Stockwell, R. G., & Coy, L. (2017). Un-
 612 expected climatological behavior of MLT gravity wave momentum flux in the
 613 lee of the Southern Andes hot spot. *Geophys. Res. Lett.*, *44*, 1182–1191. doi:
 614 10.1002/2016GL072311
- 615 Egito, F., Andrioli, V. F., & Batista, P. P. (2016). Vertical winds and momen-
 616 tum fluxes due to equatorial planetary scale waves using all-sky meteor
 617 radar over Brazilian region. *J. Atmos. Sol. Terr. Phys.*, *149*, 108–119. doi:
 618 10.1016/j.jastp.2016.10.005
- 619 Ern, M., Preusse, P., Gille, J. C., Hepplewhite, C. L., Mlynczak, M. G., Russell III,
 620 J. M., & Riese, M. (2011). Implications for atmospheric dynamics derived
 621 from global observations of gravity wave momentum flux in stratosphere and
 622 mesosphere. *J. Geophys. Res.*, *116*. doi: 10.1029/2011JD015821
- 623 Fan, Y., Klostermeyer, J., & Rüster, R. (1991). VHF radar observation of grav-
 624 ity wave critical levels in the mid-latitude summer mesopause region. *Geophys.*
 625 *Res. Lett.*, *18*, 697–700.
- 626 Forbes, J. M. (1984). Middle atmosphere tides. *J. Atmos. Terr. Phys.*(46), 1049–
 627 1067.
- 628 Fritts, D. C. (1984). Gravity wave saturation in the middle atmosphere: A review of
 629 theory and observations. *Rev. Geophys.*, *22*, 275–308.
- 630 Fritts, D. C., & Alexander, M. J. (2003). Gravity wave dynamics and ef-
 631 fects in the middle atmosphere. *Reviews of Geophysics*, *41*(1). doi:
 632 10.1029/2001RG000106
- 633 Fritts, D. C., Hoppe, U.-P., & Inhester, B. (1990). A study of the vertical motion
 634 field near the high-latitude summer mesopause during MAC/SINE. *J. Atmos.*
 635 *Terr. Phys.*, *52*, 927–938.
- 636 Fritts, D. C., Iimura, H., Lieberman, R., Janches, D., & Singer, W. (2012a). A con-

- 637 jugate study of mean winds and planetary waves employing enhanced meteor
638 radars at Rio Grande, Argentina (53.8°S) and Juliusruh, Germany (54.6°N). *J.*
639 *Geophys. Res.*, *117*. doi: 10.1029/2011JD016305
- 640 Fritts, D. C., Janches, D., & Hocking, W. K. (2010). Southern Argentina Agile Me-
641 teor Radar: Initial assessment of gravity wave momentum fluxes. *J. Geophys.*
642 *Res.*, *115*. doi: 10.1029/2010JD013891
- 643 Fritts, D. C., Janches, D., Hocking, W. K., Mitchell, N. J., & Taylor, M. J. (2012b).
644 Assessment of gravity wave momentum flux measurement capabilities by me-
645 teor radars having different transmitter power and antenna configurations. *J.*
646 *Geophys. Res.*, *117*(D10108). doi: 10.1029/2011JD017174
- 647 He, M., Chau, J. L., Stober, G., Hall, C. M., Tsutsumi, M., & Hoffmann, P. (2017).
648 Application of Manley-Rowe relation in analyzing nonlinear interactions be-
649 tween planetary waves and the solar semidiurnal tide during 2009 sudden
650 stratospheric warming event. *J. Geophys. Res.: Space Phys.*, *122*(10), 10,783-
651 10,795. doi: 10.1002/2017JA024630
- 652 Hines, C. O. (1988). A modeling of atmospheric gravity waves and wave drag gener-
653 ated by isotropic and anisotropic terrain. *J. Atmos. Sci.*, *45*, 309–322.
- 654 Hocking, W. K. (2005). A new approach to momentum flux determinations using
655 SKiYMET meteor radars. *Annales Geophysicae*, *23*(7), 2433–2439. doi: 10
656 .5194/angeo-23-2433-2005
- 657 Hocking, W. K., Fuller, B., & Vandeppeer, B. (2001). Real-time determination of
658 meteor-related parameters utilizing modern digital technology. *J. Atmos. Sol.-*
659 *Terr. Phy.*(63), 155–169. doi: 10.1016/S1364-6826(00)00138-3
- 660 Hocking, W. K., & Thayaparan, T. (1997). Simultaneous and collocated observa-
661 tions of winds and tides by MF and meteor radars over london, canada (43°N,
662 81°W), during 1994–1996. *Radio Science*, *32*(2), 833–865.
- 663 Hoffmann, P., Becker, E., Singer, W., & Placke, M. (2010). Seasonal variation of
664 mesospheric waves at northern middle and high latitudes. *J. Atmos. Sol.-Terr.*
665 *Phy.*, *72*(14-15), 1068–1079. doi: 10.1016/j.jastp.2010.07.002
- 666 Holdsworth, D. A., Reid, I. M., & Cervera, M. A. (2004). Buckland park all-sky in-
667 terferometric meteor radar. *Radio Sci.*, *39*(5). doi: 10.1029/2003RS003014
- 668 Jacobi, C., Portnyagin, Y. I., Solovjova, T. V., Hoffmann, P., Singer, W., Fahrutdi-
669 nova, A. N., ... Meek, C. E. (1999). Climatology of the semidiurnal tide at
670 52–56°N from ground-based radar wind measurements 1985–1995. *J. Atmos.*
671 *Sol.-Terr. Phy.*, *61*(13), 975–991. doi: 10.1016/S1364-6826(99)00065-6
- 672 Jia, M., Xue, X., Gu, S., Chen, T., Ning, B., Wu, J., ... Dou, X. (2018). Multiyear
673 observations of gravity wave momentum fluxes in the midlatitude mesosphere
674 and lower thermosphere region by meteor radar. *J. Geophys. Res.*, *123*, 5684–
675 5703. doi: 10.1029/2018JA025285
- 676 Jones, J., Webster, A. R., & Hocking, W. K. (1998). An improved interferome-
677 ter design for use with meteor radars. *Radio Sci.*, *33*, 55–65. doi: 10.1029/
678 97RS03050
- 679 Kudeki, E., & Franke, S. J. (1998). Statistics of momentum flux estimation. *J. At-*
680 *mos. Sol.-Terr. Phy.*, *60*, 1549–1553.
- 681 Kumar, K. K., Subrahmanyam, K. V., Mathew, S. S., Koushik, N., & Ramkummar,
682 G. (2018). Simultaneous observations of the quasi 2-day wave climatology over
683 the low and equatorial latitudes in the mesosphere lower thermosphere. *Clim.*
684 *Dyn.*, *51*, 221–233. doi: 10.1007/s00382-017-3916-2
- 685 Laskar, F. I., Chau, J. L., Stober, G., Hoffmann, P., Hall, C. M., & Tsutsumi, M.
686 (2016). Quasi-biennial oscillation modulation of the middle- and high-latitude
687 mesospheric semidiurnal tides during August–September. *J. Geophys. Res.:
688 Space Phys.*, *121*(5), 4869–4879. doi: 10.1002/2015JA022065
- 689 Lindzen, R. S., & Chapman, S. (1969). Atmospheric tides. *Space Sci. Rev.*, *10*, 3–
690 188.
- 691 Liu, A. Z., Lu, X., & Franke, S. J. (2013). Diurnal variation of gravity wave mo-

- 692 momentum flux and its forcing on the diurnal tide. *J. Geophys. Res.*, *118*, 1668–
693 1678.
- 694 Liu, H.-L., & Roble, R. G. (2002). A study of a self-generated stratospheric sudden
695 warming and its mesospheric-lower thermospheric impacts using the coupled
696 TIME-GCM/CCM3. *J. Geophys. Res.*, *107*. doi: 10.1029/2001JD001533
- 697 Lu, X., Chu, X., Li, H., Chen, C., Smith, J. A., & Vadas, S. L. (2017). Statistical
698 characterization of high-to-medium frequency mesoscale gravity waves by lidar-
699 measured vertical winds and temperatures in the MLT. *J. Atmos. Sol.-Terr.*
700 *Phys.*, *162*, 3–15. doi: 10.1016/j.jastp.2016.10.009
- 701 Lund, T., Fritts, D., Kam, W., Laughman, B., & Liu, H.-L. (2020). Numerical sim-
702 ulation of mountain waves over the Southern Andes, Part 1: Mountain wave
703 and secondary wave character, evolutions, and breaking. *J. Atm. Sci.*.
- 704 McCormack, J. P., Coy, L., & Singer, W. (2014). Intraseasonal and inter-
705 annual variability of the quasi 2 day wave in the Northern Hemisphere
706 summer mesosphere. *J. Geophys. Res. Atmos.*, *119*, 2928–2946. doi:
707 10.1002/2013JD020199
- 708 Meriwether, J., Faivre, M., Fesen, C., Sherwood, P., & Veliz, O. (2008). New results
709 on equatorial thermospheric winds and the midnight temperature maximum.
710 *Ann. Geophys.*, *26*, 447–466.
- 711 Murphy, D. J., Forbes, J. M., Walterscheid, R. L., Hagan, M. E., Avery, S. K.,
712 Aso, T., ... Vincent, R. A. (2006). A climatology of tides in the antarctic
713 mesosphere and lower thermosphere. *J. Geophys. Res.*, *111*. doi:
714 10.1029/2005JD006803
- 715 Offermann, D., Hoffmann, P., Knieling, P., Koppmann, R., Oberheide, J., Rigglin,
716 D. M., ... Steinbrecht, W. (2011). Quasi 2 day waves in the summer meso-
717 sphere: Triple structure of amplitudes and long-term development. *J. Geophys.*
718 *Res.*, *116*. doi: 10.1029/2010JD015051
- 719 Orte, P. F., Wolfram, E., Salvador, J., Mizuno, A., Bègue, N., Bencherif, H., ...
720 Quiroga, J. (2019). Analysis of a southern sub-polar short-term ozone varia-
721 tion event using a millimetre-wave radiometer. *Ann. Geophys.*, *37*, 613–629.
722 doi: 10.5194/angeo-37-613-2019
- 723 Pancheva, D., & Mukhtarov, P. (2011). Atmospheric tides and planetary waves:
724 recent progress based on SABER/TIMED temperature measurements
725 (2002–2007). *Aeronomy of the Earth's Atmosphere and Ionosphere, IAGA*
726 *Special Sopron Book Series 2*. doi: 10.1007/978-94-007-0326-1_2
- 727 Piani, C., Durran, D., Alexander, M. J., & Holton, J. R. (2000). A numerical study
728 of three-dimensional gravity waves triggered by deep tropical convection and
729 their role in the dynamics of the QBO. *J. Atmos. Sci.*, *57*, 3689–3702. doi:
730 10.1029/2019EA000570
- 731 Placke, M., Hoffmann, P., Becker, E., Jacobi, C., Singer, W., & Rapp, M. (2011b).
732 Gravity wave momentum fluxes in the MLT—Part II: Meteor radar investiga-
733 tions at high and midlatitudes in comparison with modeling studies. *J. Atmos.*
734 *Sol. Terr. Phys.*, *73*, 911–920. doi: 10.1016/j.jastp.2010.05.007
- 735 Placke, M., P. Hoffmann, P., Latteck, R., & Rapp, M. (2015). Gravity wave momen-
736 tum fluxes from MF and meteor radar measurements in the polar MLT region.
737 *J. Geophys. Res.*, *120*, 736–750. doi: 10.1002/2014JA020460
- 738 Placke, M., Stober, G., & Jacobi, C. (2011a). Gravity wave momentum fluxes in
739 the MLT—Part I: seasonal variation at Collm (51.3°N, 13.0°E). *J. Atmos. Sol.*
740 *Terr. Phys.*, *73*, 904–910. doi: 10.1016/j.jastp.2010.05.007
- 741 Rossby, C.-G. (1939). Relation between variations in the intensity of the zonal cir-
742 culation of the atmosphere and the displacements of the semipermanent centers
743 of action. *J. Mar. Res.*, *2*, 38–55.
- 744 Sandford, D. J., Muller, H. G., & Mitchell, N. J. (2006). Observations of lunar tides
745 in the mesosphere and lower thermosphere at Arctic and middle latitudes. *At-*
746 *mos. Chem. Phys.*, *6*, 4117–4127.

- 747 Siddiqui, T. A., Maute, A., Pedatella, N., Yamazaki, Y., Lühr, H., & Stolle, C.
748 (2018). On the variability of the semidiurnal solar and lunar tides of the equa-
749 torial electrojet during sudden stratospheric warmings. *Ann. Geophys.*, *36*,
750 1545–1562. doi: 10.5194/angeo-2018-80
- 751 Smith, A. K. (2012). Global dynamics of the MLT. *Surveys in Geophysics*, *33*(6),
752 1177–1230.
- 753 Spargo, A. J., Reid, I. M., & MacKinnon, A. D. (2019). Multistatic me-
754 teor radar observations of gravity-wave–tidal interaction over southern
755 Australia. *Atmospheric Measurement Techniques*, *12*, 4791–4812. doi:
756 10.5194/amt-12-4791-2019
- 757 Stening, R. J., Forbes, J. M., Hagan, M. E., & Richmond, A. D. (1997). Exper-
758 iments with a lunar atmospheric tidal model. *J. Geophys. Res.*, *102*, 13,465–
759 13,472. doi: 10.1029/97JD00778
- 760 Stober, G., & Chau, J. L. (2015). A multistatic and multifrequency novel approach
761 for specular meteor radars to improve wind measurements in the mlr region.
762 *Radio Sci.*, *50*, 431–442. doi: 10.1002/2014RS005591
- 763 Thorsen, D., Franke, S. J., & Kudeki, E. (1997). A new approach to MF radar inter-
764 ferometry for estimating mean winds and momentum flux. *Radio Sci.*, *32*(2),
765 707–726.
- 766 Trinh, Q. T., Ern, M., Doornbos, E., Preusse, P., & Riese, M. (2018). Charac-
767 teristics of the quiet-time hot spot gravity waves observed by GOCE over
768 the Southern Andes on 5 July 2010. *Ann. Geophys.*, *36*, 425–444. doi:
769 10.5194/angeo-36-425-2018
- 770 Urco, J. M., Chau, J. L., Milla, M. A., Vierinen, J., & Weber, T. (2018). Coherent
771 MIMO to improve aperture synthesis radar imaging of field-aligned irregulari-
772 ties: First results at Jicamarca. *IEEE Transactions on Geoscience and Remote
773 Sensing*, *PP*(99), 1–11. doi: 10.1109/TGRS.2017.2788425
- 774 Urco, J. M., Chau, J. L., Weber, T., & Latteck, R. (2019). Enhancing the spatio-
775 temporal features of polar mesosphere summer echoes using coherent MIMO
776 and radar imaging at MAARSY. *Atmospheric Measurement Techniques*, *12*,
777 955–969. doi: 10.5194/amt-12-955-2019
- 778 Vadas, S. L., & Becker, E. (2019). Numerical modeling of the generation of tertiary
779 gravity waves in the mesosphere and thermosphere during strong mountain
780 wave events over the Southern Andes. *J. Geophys. Res.*, *124*, 7687–7718. doi:
781 10.1029/2019JA026694
- 782 Vadas, S. L., Xu, S., Yue, J., Bossert, K., Becker, E., & Baumgarten, G. (2019a).
783 Characteristics of the quiet-time hot spot gravity waves observed by GOCE
784 over the Southern Andes on 5 July 2010. *J. Geophys. Res.*, *124*, 7034–7061.
785 doi: 10.1029/2019JA026693
- 786 Vierinen, J., Chau, J. L., Charuvil, H., Urco, J. M., Clahsen, M., Avsarkisov, V.,
787 ... Volz, R. (2019). Observing mesospheric turbulence with specular meteor
788 radars: A novel method for estimating second-order statistics of wind velocity.
789 *Earth and Space Science*, *6*, 1171–1195. doi: 10.1029/2019EA000570
- 790 Vierinen, J., Chau, J. L., Pfeffer, N., Clahsen, M., & Stober, G. (2016). Coded con-
791 tinuous wave meteor radar. *Atmospheric Measurement Techniques*, *9*(2), 829–
792 839.
- 793 Vincent, R. A., Kovalam, S., Reid, I. M., & Younger, J. P. (2010). Gravity wave
794 flux retrievals using meteor radars. *Geophys. Res. Lett.*, *37*. doi: 10.1029/
795 2010GL044086
- 796 Wilhelm, S., Stober, G., & Brown, P. (2019). Climatologies and long-term
797 changes in mesospheric wind and wave measurements based on radar ob-
798 servations at high and mid latitudes. *Ann. Geophys.*, *37*, 851–875. doi:
799 10.5194/angeo-37-851-2019
- 800 Yamazaki, Y., Matthias, V., Miyoshi, Y., Stolle, C., Siddiqui, T., Kervalishvili, G.,
801 ... Alken, P. (2020). September 2019 antarctic sudden stratospheric warming:

802
803

Quasi-6-day wave burst and ionospheric effects. *Geophys. Res. Lett.*, 47. doi:
10.1029/2019GL086577